# Chapter 2: Changes in Atmospheric Constituents and in Radiative Forcing

**Coordinating Lead Authors:** Piers Forster, V. Ramaswamy

**Lead Authors:** Paulo Artaxo, Terje Berntsen, Richard Betts, Dave Fahey, Jim Haywood, Judith Lean, Dave Lowe, Gunnar Myhre, John Nganga, Ronald Prinn, Graciela Raga, Michael Schulz, Rob Van Dorland

**Contributing Authors:** Greg Bodeker (New Zealand), Olivier Boucher (France), William Collins (USA), Thomas J. Conway (USA), Ed Dlugokencky (USA), Jim Elkins (USA), David Etheridge (Australia), Paul Fraser (Australia), Dave Keeling (USA), Ralph Keeling (USA), Stefan Kinne (Germany), Keith Lassey (New Zealand), Ulrike Lohmann (Switzerland), Andrew Manning (UK), Steve Montzka (USA), David Oram (UK), Kath O'Shaughnessy (New Zealand), Steve Piper (USA), Michael Ponater (Germany), Navin Ramankutty (India), Karen Rosenlof (USA), Robert Sausen (Germany), Dan Schwarzkopf (USA), Georgiy Stenchikov (USA), Nicola Stuber (Germany), Toshihiko Takemura (Japan). Christiane Textor (France), Ray Wang (USA), Ray Weiss (USA), Tim Whorf (USA).

**Review Editors:** Teruyuki Nakajima (Japan), V. Ramanathan (USA)

**Date of Draft:** 27 February 2006

**Notes:** TSU compiled version

**Figures**

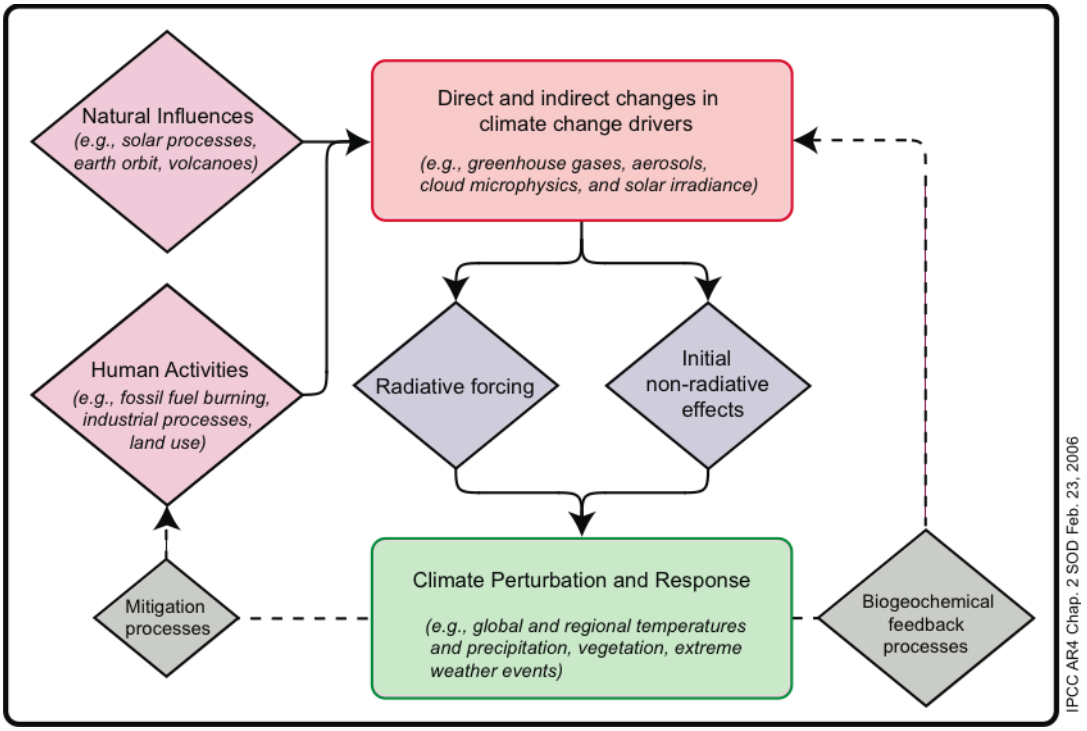


**Figure 2.1.** Flow diagram illustrating how RF links to other areas of climate change being assessed in this report.

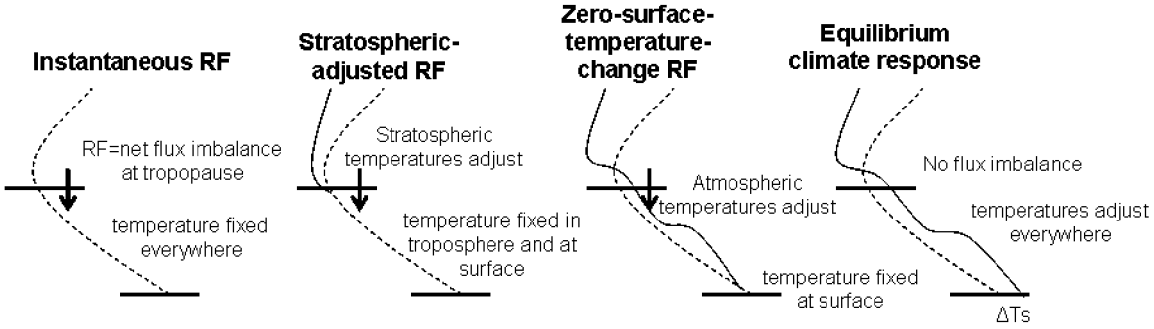


**Figure 2.2**. Cartoon comparing: instantaneous RF; stratospheric-adjusted RF, which allows stratospheric temperatures to adjust; zero-surface-temperature-change RF, which allows atmospheric temperatures to adjust; and $\Delta T_s$, the equilibrium surface temperature response to the forcing agent, as calculated by a GCM. Based on Hansen et al. (2005).

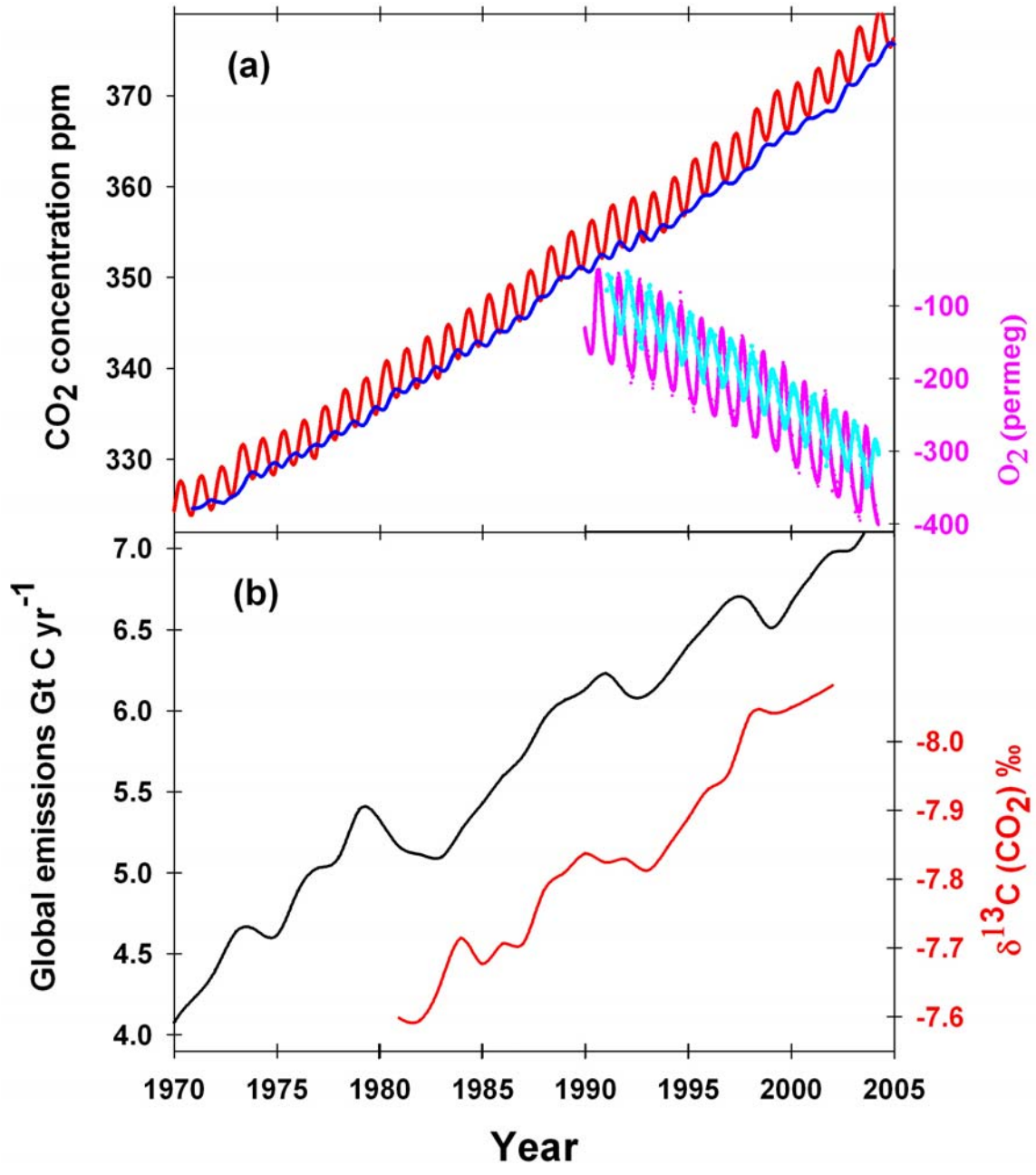


**Figure 2.3.** Panel (a) shows $CO_2$ concentrations (monthly averages) measured by continuous analyser over the period 1970 to 2004 for Mauna Loa (19°N red) (Keeling and Whorf, 2005) and Baring Head (41°S blue) (following techniques by Manning et al., 1997). Due to the larger amount of terrestrial biosphere in the Northern hemisphere, seasonal cycles in $CO_2$ are larger there than in the Southern hemisphere. In the lower right of the panel, atmospheric oxygen measurements are shown from Alert, Canada (pink) and Cape Grim (41°S cyan) (Manning and Keeling, 2005).The $O_2$ concentration is measured as the "permeg" (parts per million) deviations in the $O_2/N_2$ ratio from a calibration standard. Panel (b) shows the annual global $CO_2$ emissions from fossil-fuel burning and cement manufacture GtC $yr^{-1}$ (black) through to 2002. Data from the CDIAC website (Marland et al., 2005). Preliminary emissions data for 2003 and 2004 of 7.0 and 7.2 Gt C $yr^{-1}$ respectively are derived from BP Statistical Review of World Enegy 2005 website. Annual averages of the $^{13}C/^{12}C$ ratio measured in atmospheric $CO_2$ at Mauna Loa from 1981 to 2002 (red) are also shown (Keeling et al., 2005). The isotope data are expressed as $\delta^{13}C(CO_2)$ "‰" (parts per thousand) deviation from a calibration standard.

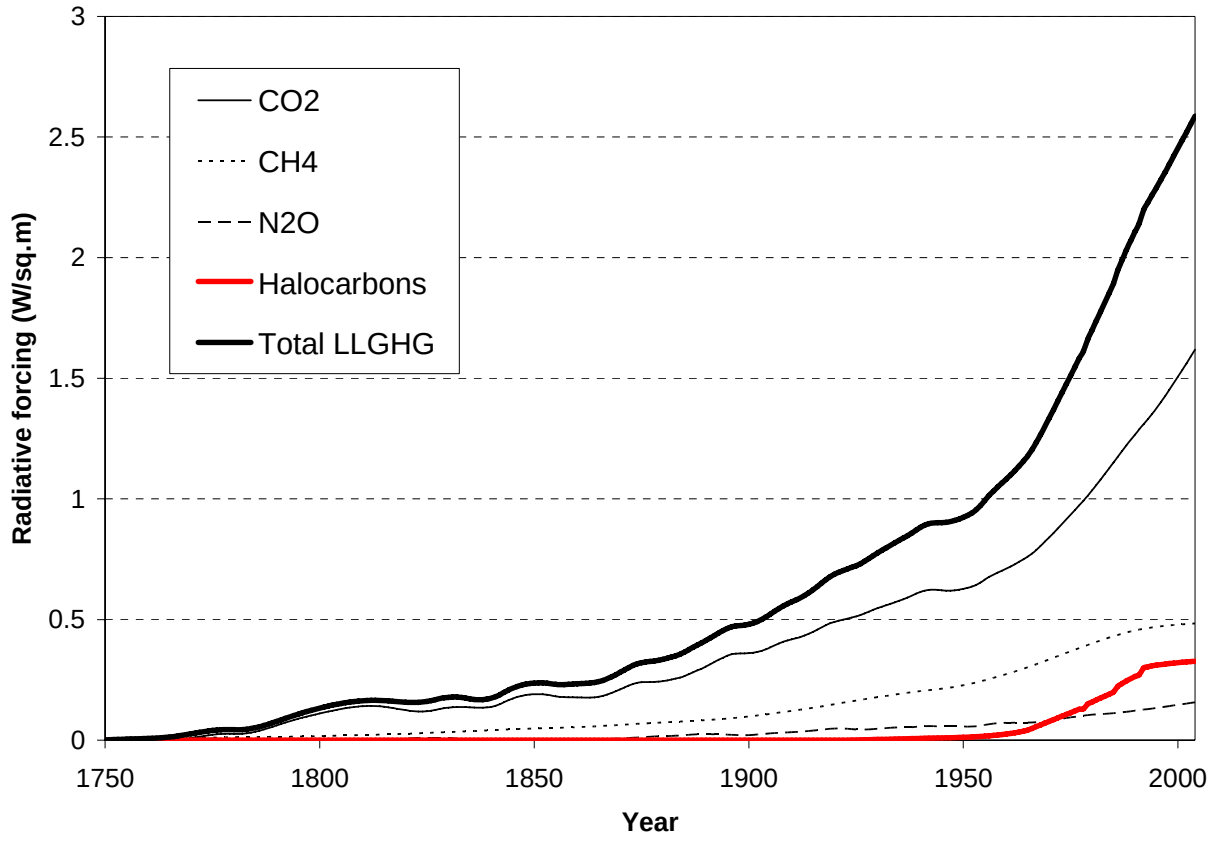


**Figure 2.4.** Timeseries of LLGHG radiative forcings constructed from observed gas concentrations. The concentrations are based on the several datasets from ice-cores, firn air, flask and *in-situ* measurements discussed in Section 2.3, see also McFarling Meure (2004).

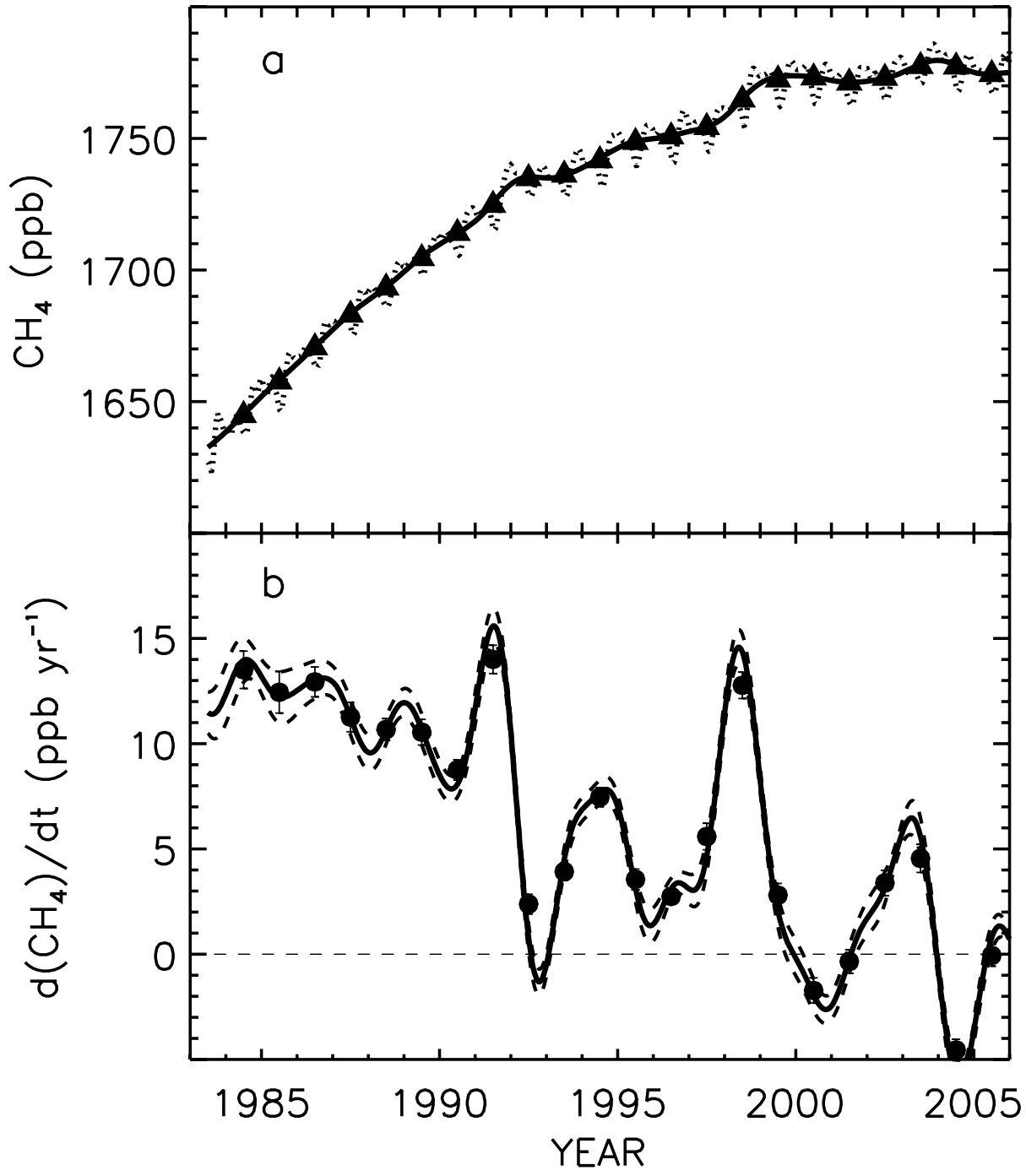


**Figure 2.5.** (a) Trend in global methane abundance (mole fraction in ppb) derived from surface sites operated by NOAA/ESRL. The dashed line shows the methane global averages and the solid line is the deseasonlised global average trend. The triangles are the global annual means plotted in the middle of the year (b) Instantaneous annual growth rate (ppb $yr^{-1}$) in global atmospheric methane abundance from 1984 through to mid 2005 calculated as the derivative of the deseasonalized trend curve in (a) above (solid line). The annual increases (solid circles) are from 1 January to 1 January the following year. The dashed lines show one standard deviation uncertainties for the instantaneous growth rate calculated with a Monte Carlo simulation. (Note that in the next draft of the AR4 this figure will provide both AGAGE and NOAA/ESRL methane data through to the end of 2005).

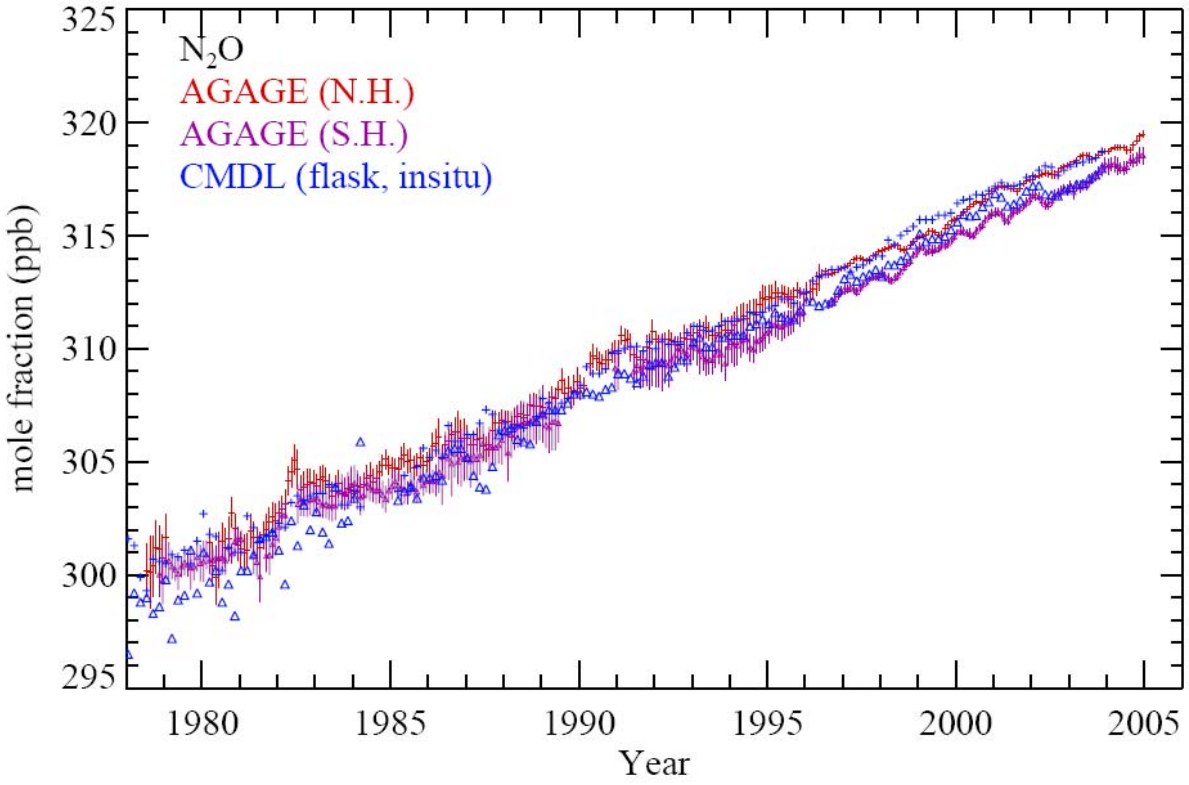


**Figure 2.6.** Hemispheric monthly mean $N_2O$ mole fractions (crosses for northern and triangles for Southern Hemisphere). Observations (*in-situ*) of $N_2O$ from ALE and GAGE (through mid-1990s) and AGAGE (since mid-1990s) (Prinn et al., 2000; Prinn et al., 2005b) are shown with monthly standard deviations. Data from CMDL are shown without these standard deviations (Thompson et al., 2004).

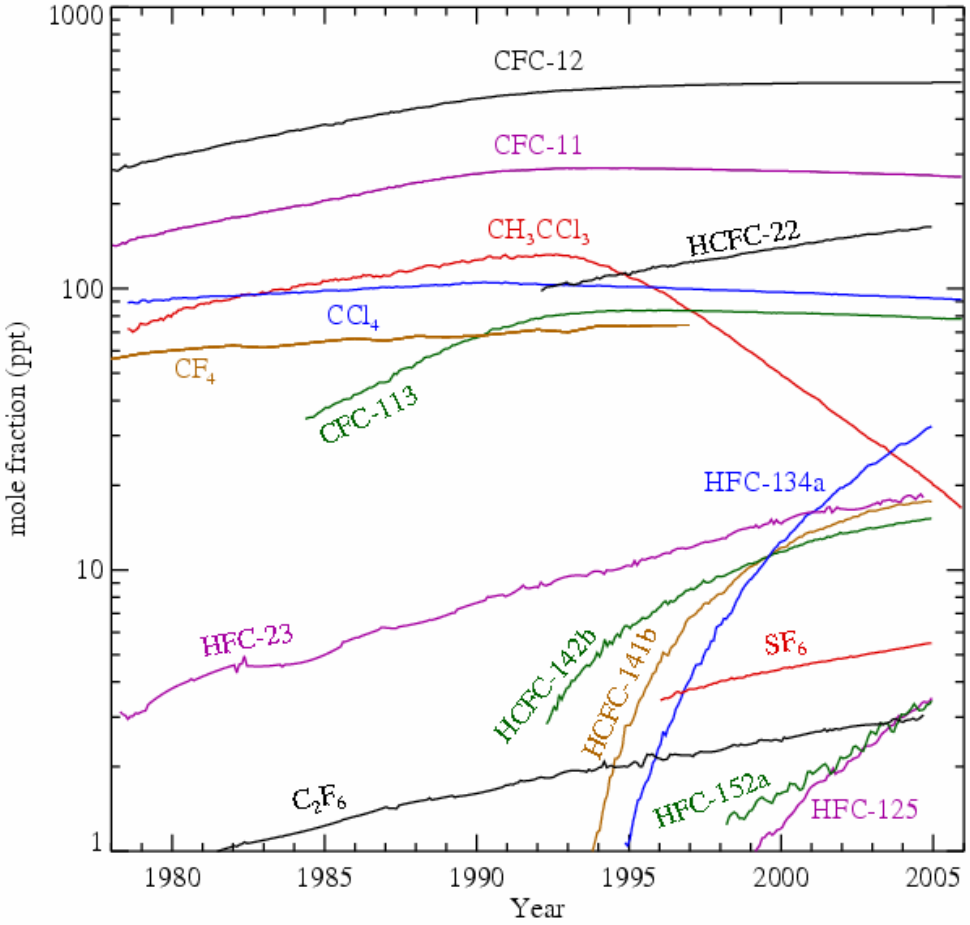


**Figure 2.7.** Temporal evolution of the global-average dry-air mole fractions (parts per trillion, ppt) of the major halogen-containing LLGHGs. These are derived using monthly-mean measurements from the AGAGE and NOAA-GMD networks averaged with equal weight where both are available. While differences exist, these network measurements agree reasonably well with each other, and with other measurements where available (see text for references).

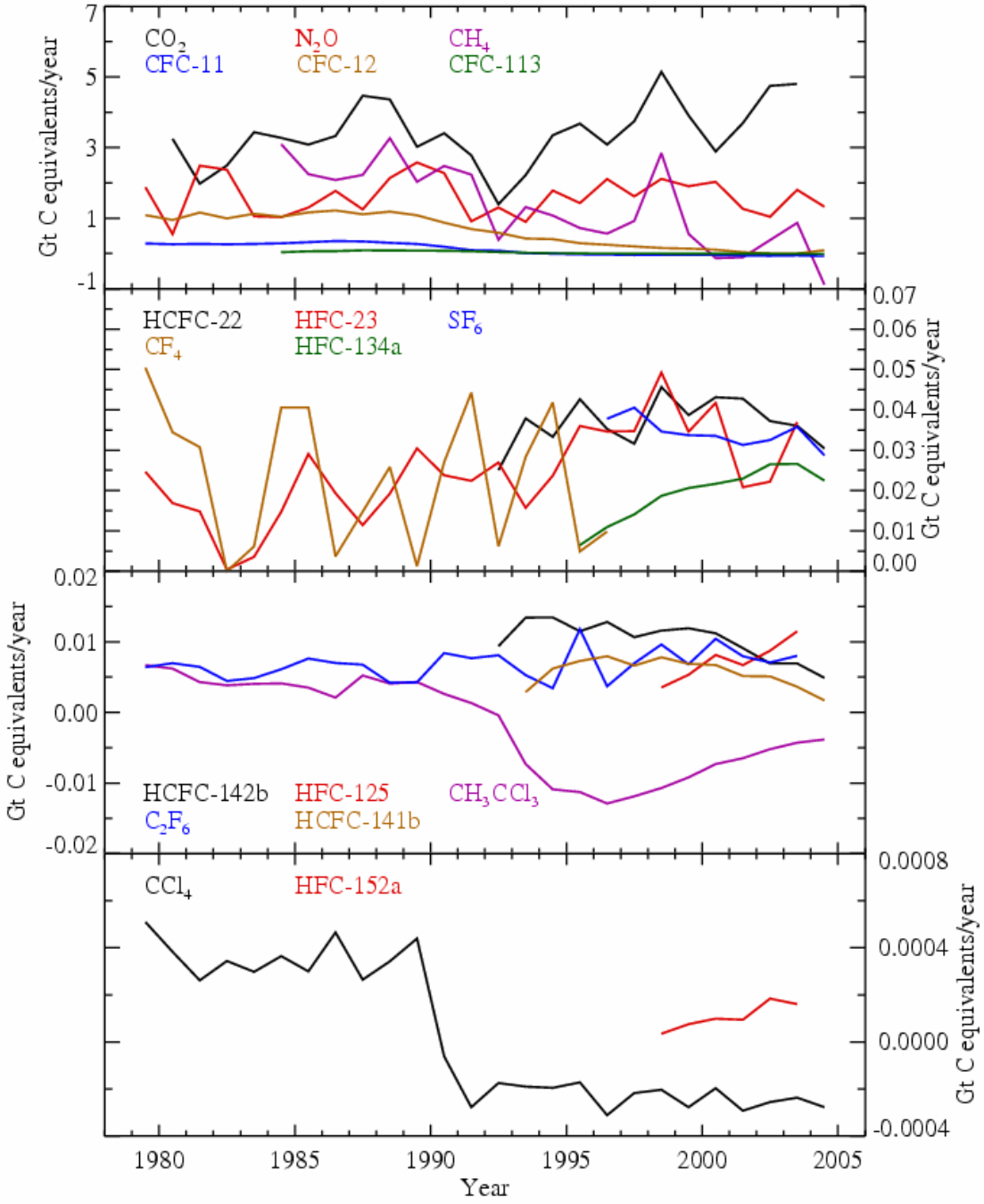


**Figure 2.8.** Annual rates of change of the global atmospheric masses of each of the major LLGHGs expressed in common units of GtC $yr^{-1}$. These rates are computed from their actual annual mass changes in Gt/year (as derived from their observed global- and annual-average mole fractions discussed in Sections 2.3.1–2.3.4) by multiplying them by their global warming potentials for 100-year time horizons and then dividing by the ratio of the $CO_2$ to C masses (44/12). These rates are positive/negative whenever the mole fractions are increasing/decreasing, respectively. Use of these common units provides an approximate way to intercompare the fluxes of LLGHGs using the same approach used to intercompare the values of various LLGHG emission reductions under the Kyoto Protocol (see e.g., Prinn, 2004).

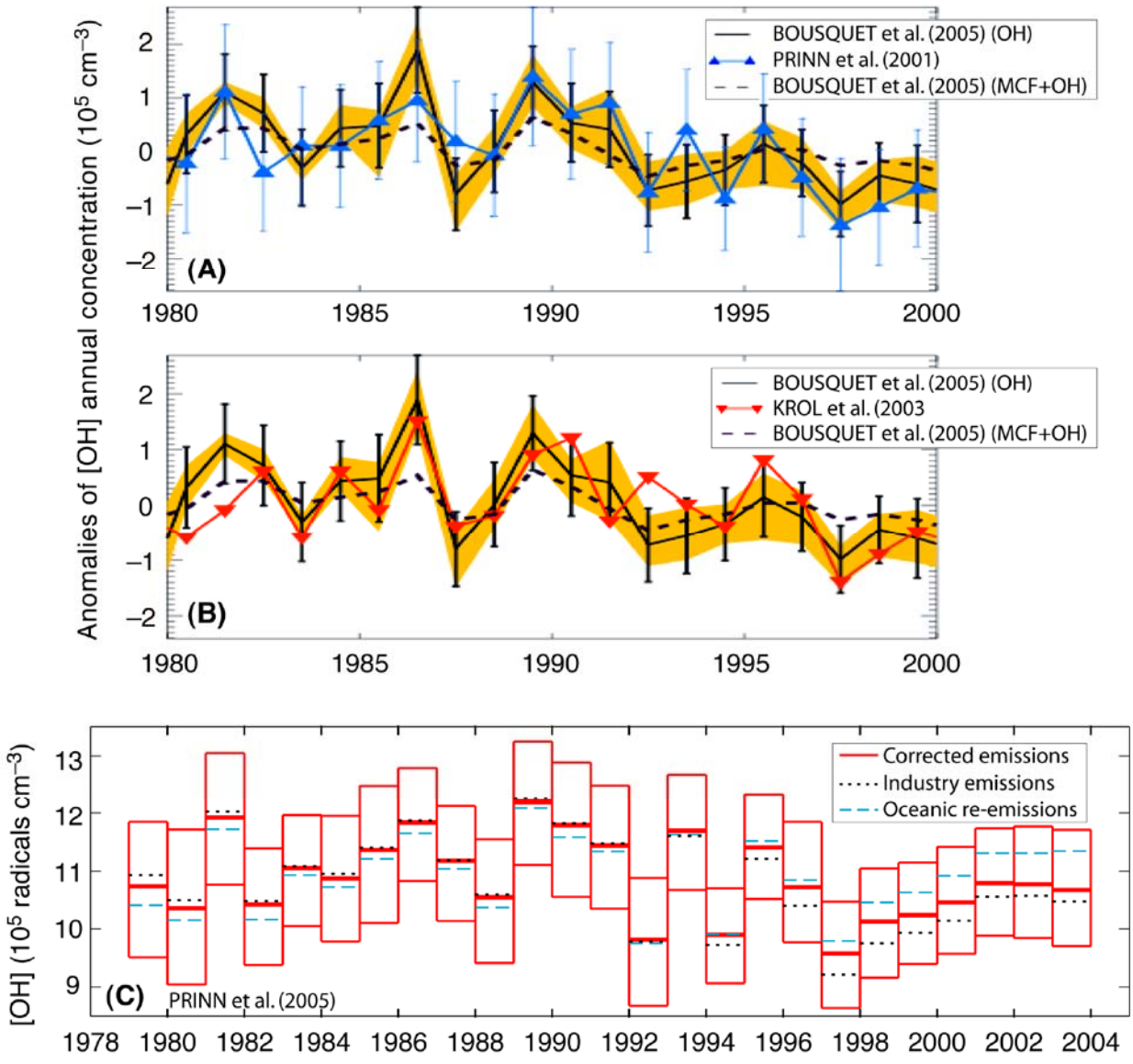


**Figure 2.9.** Estimates of trends in weighted global-average OH concentrations. (A) and (B): comparison of 1980–1999 OH anomalies (relative to their long-term means) inferred by Bousquet et al (2005), Prinn et al. (2001) and Krol et al. (2003) from AGAGE methyl chloroform (MCF) observations, and by Bousquet et al. (2005) when $CH_3Cl_3$ emissions as well as OH are inferred; error bars for Bousquet et al. (2005) refer to 1-sigma inversion errors while yellow areas refer to envelope of their 18 OH inversions. (C) OH concentrations for 1979–2003 inferred by Prinn et al. (2005a) utilizing industry emissions corrected using recent $CH_3Cl_3$ observations which show the recovery of 2003 OH levels to 1979 levels; also shown are results assuming uncorrected emissions and estimates of recent oceanic re-emissions. Error bars in Prinn et al. (2001, 2005a) are 1-sigma and include inversion, model, emission and calibration errors from large Monte Carlo ensembles (see Section 2.3.5 for details and references).

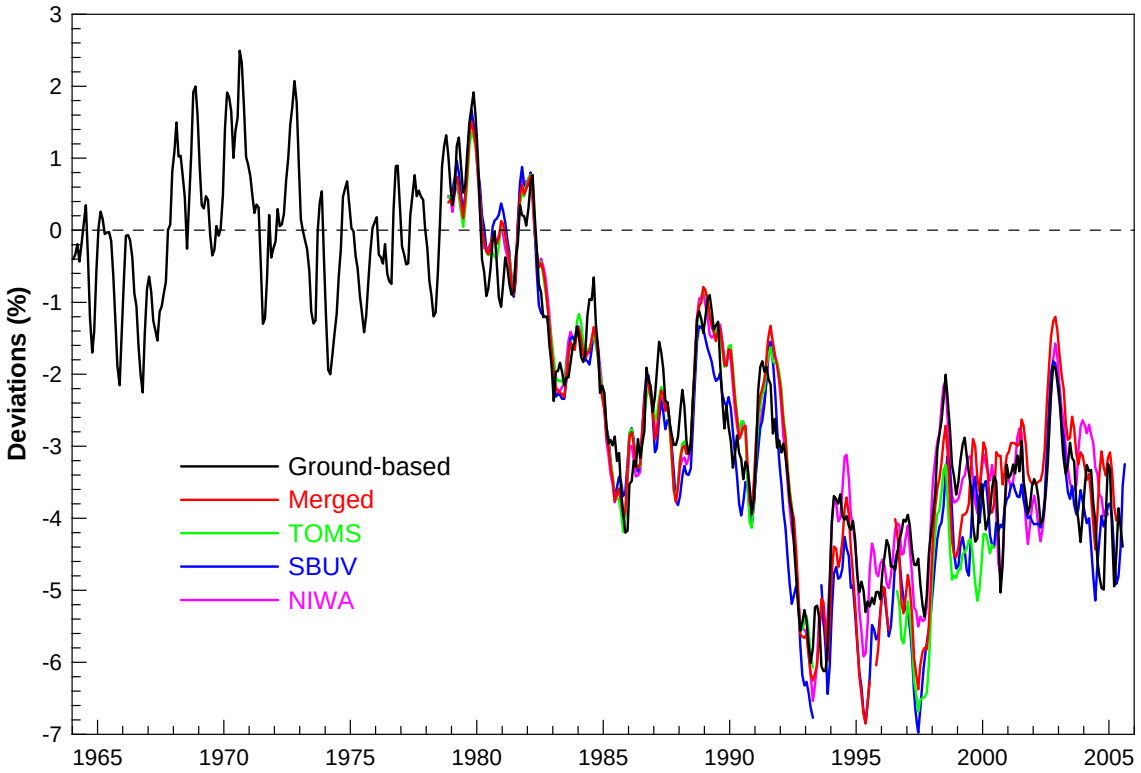


**Figure 2.10.** Time series of deseasonalized global mean total column ozone anomalies estimated from five different data sets. Ground-based (black line) and satellite-based (coloured lines) measurements are included. First the seasonal cycle is removed from each data set, and the deviations are then area-weighted and expressed as anomalies with respect to the period 1964–1980. Updated from Fioletov et al. (2002).

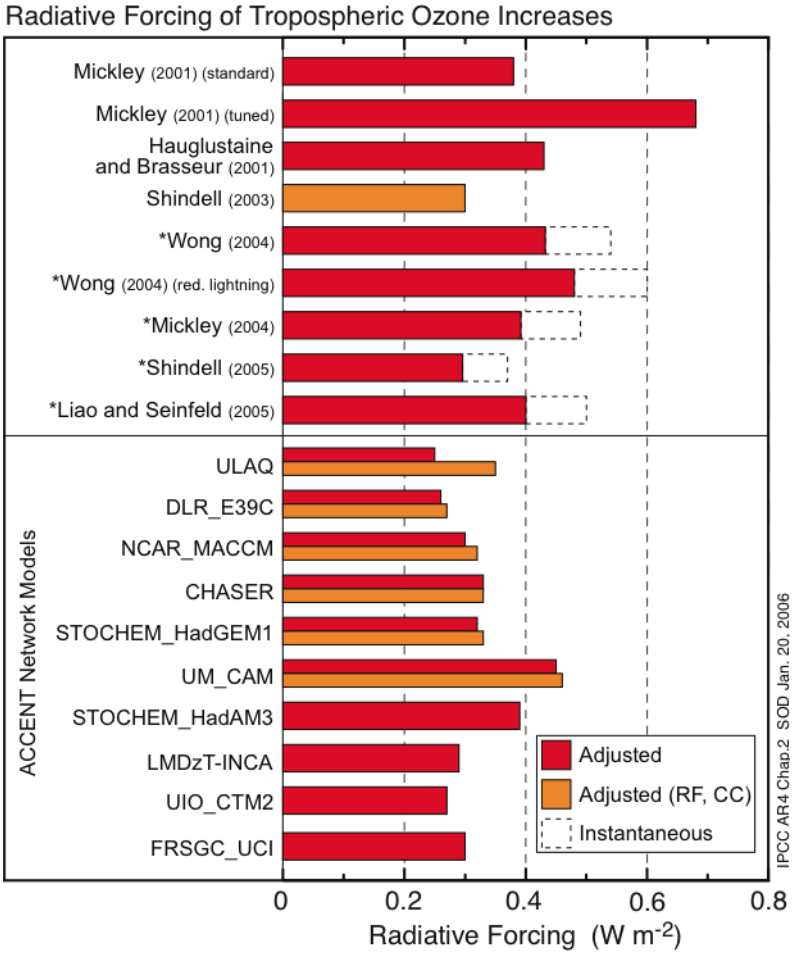


**Figure 2.11.** Calculated radiative forcing due to tropospheric ozone change since pre- industrial time based on CTM and GCM model simulations published since the TAR. Estimates with GCMs including the effect of climate change since 1750 are given by orange bars (Adjusted RF, CC). Studies denoted with an (*) give only instantaneous RF in the original publications. Adjusted RF for these is estimated by reducing the instantaneous RF (indicated by the dashed bars) by 20%. The instantaneous RF from Mickley et al. (2001) is reported as adjusted RF in Gauss et al. (2006).

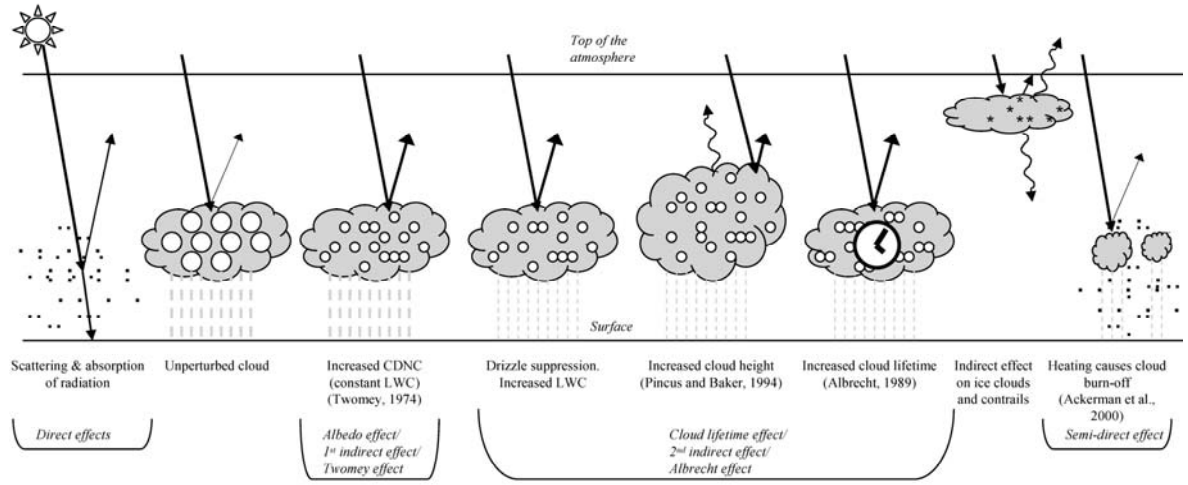


**Figure 2.12.** Schematic diagram showing the various radiative forcing mechanisms that have been identified as significant (modified from Haywood and Boucher, 2000). The small black dots represent aerosol particles, the larger open circles cloud droplets. Straight lines represent the incident and reflected solar radiation and wavy lines represent terrestrial radiation. The unperturbed cloud contains larger cloud drops as only natural aerosols are available as cloud condensation nuclei (CCN, CDCN on Figure), while the perturbed cloud contains a greater number of smaller cloud drops as both natural and anthropogenic aerosols are available as CCN. The vertical grey dashes represent rainfall. LWC is the liquid water content.

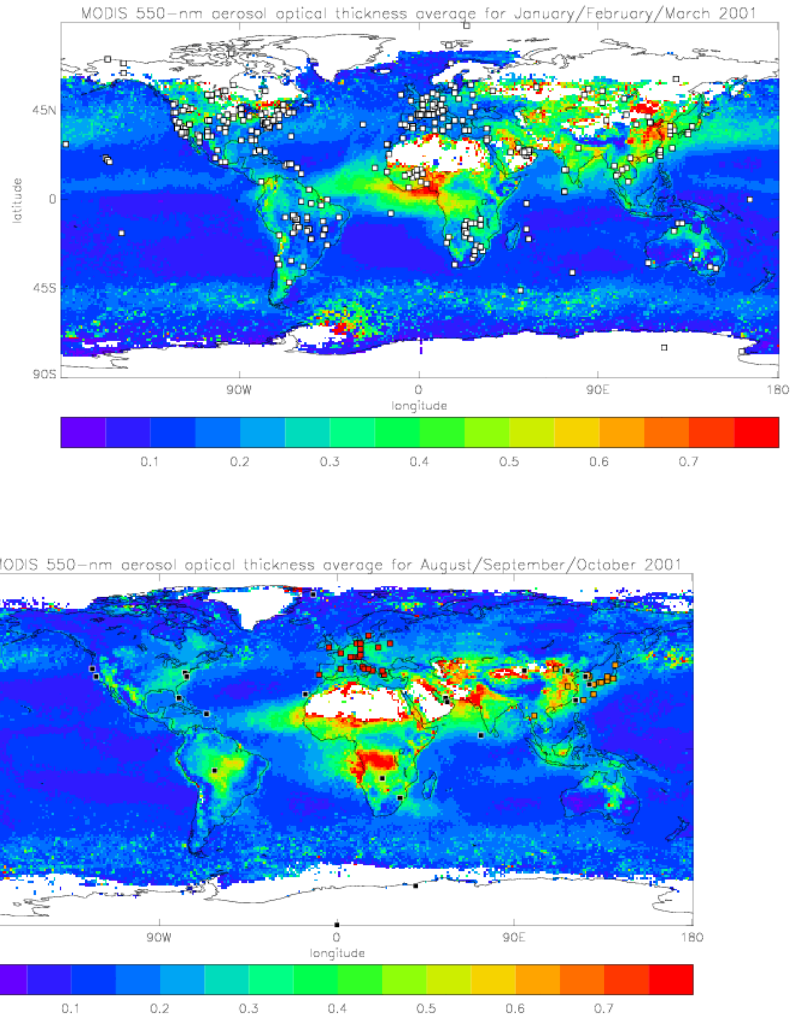


**Figure 2.13.** The $\tau_{aer}$ at 550 nm determined by the MODIS instrument for (a) January/February/March 2001, (b) for August/September/October 2001. a) Shows the location of AERONET sites that have been operated since 1996. b) Shows the location of different aerosol lidar networks (red = EARLINET, orange = ADNET, black = MPLNET).

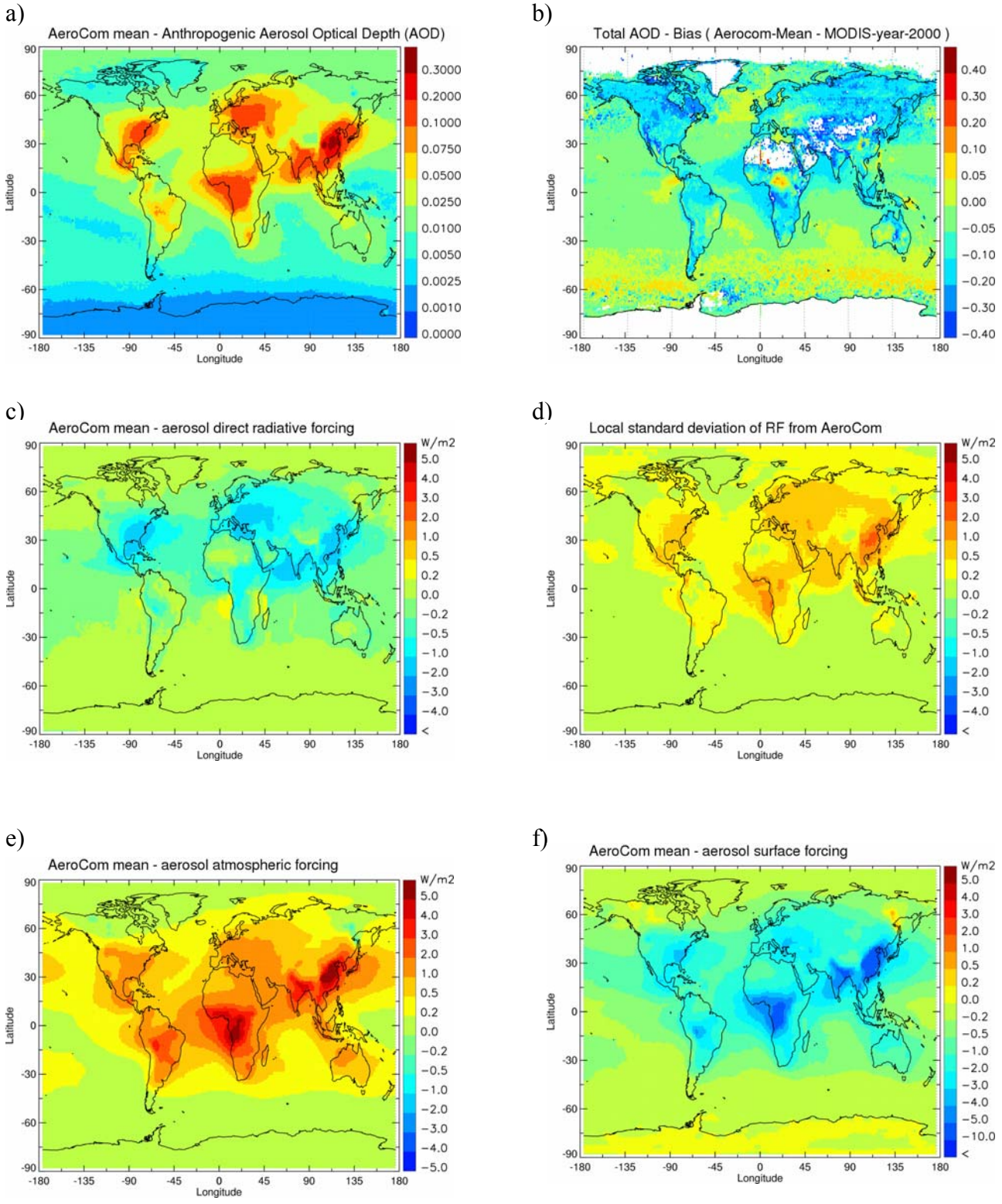


**Figure 2.14.** (a) Mean anthropogenic aerosol optical depth derived from 9 AeroCom models corresponding to Table 2. 5. (b) Difference in total aerosol optical depth between AeroCom mean and MODIS satellite product year 2000. (c) Mean short wave RF from AeroCom models. (d) Local standard deviation of RF using simulated RF fields from 9 AeroCom models. (e) Mean atmospheric forcing from AeroCom models. (f) Mean surface forcing from AeroCom models.

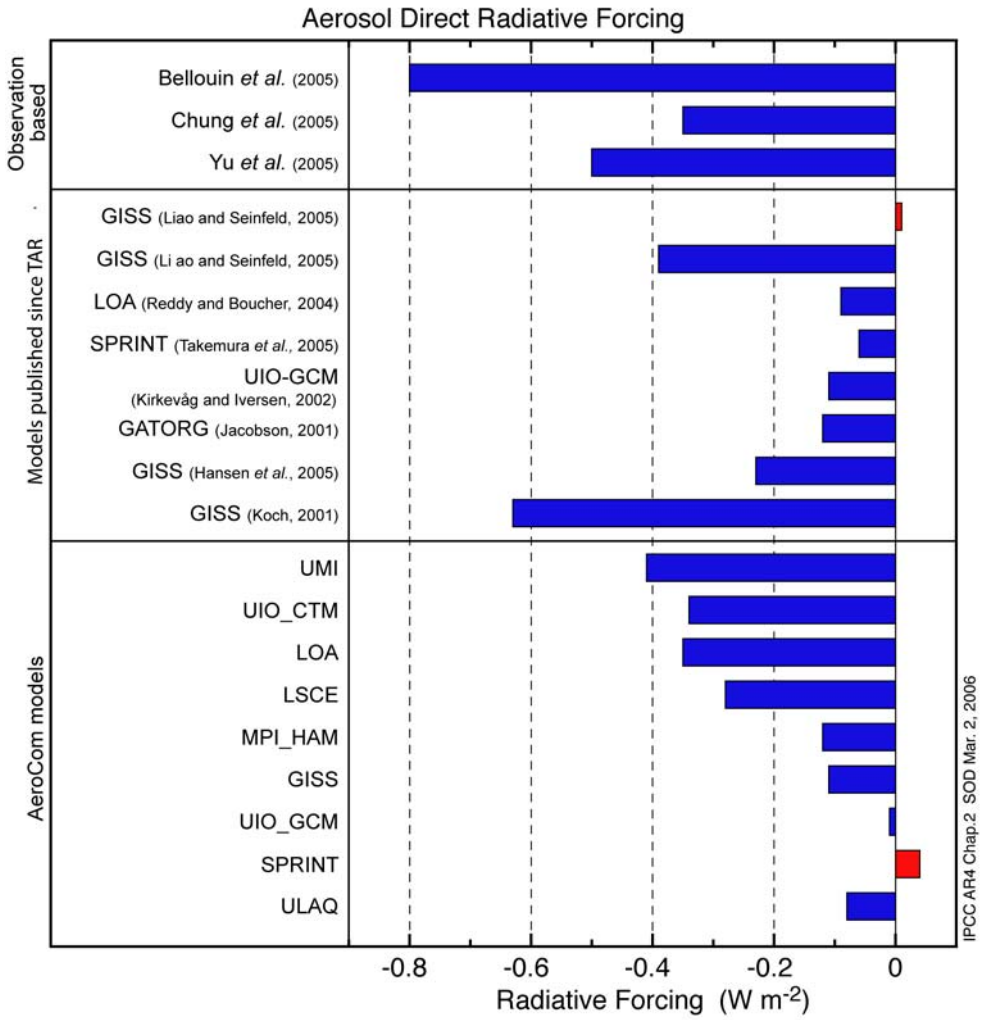


**Figure 2.15.** Estimates of the direct aerosol RF since TAR from observational based studies, published modelling studies, and AEROCOM results with identical aerosol and aerosol precursor emissions. Separate results for external and internal mixture are shown from Liao and Seinfeld (2005).

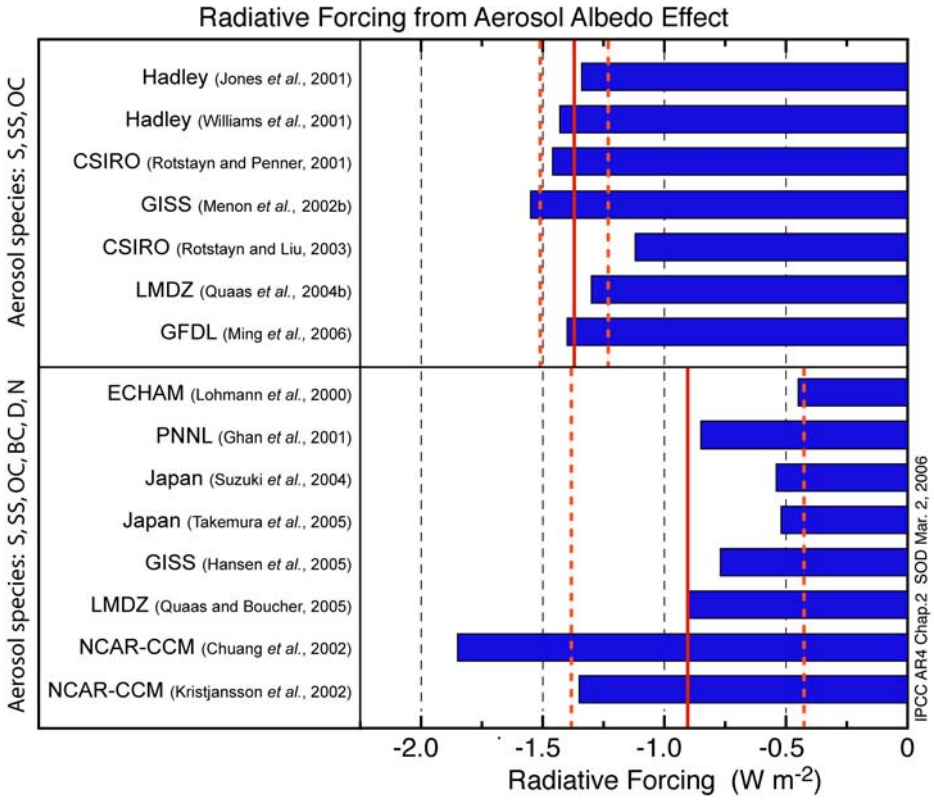


**Figure 2.16.** Radiative forcing due to the albedo effect from the global climate models that appear in the shaded boxes in Table 2.7. The labels next to the bars correspond to the published study, while the labels in the horizontal axis at the top of the boxes indicate the institute/university/agency or country with which each model is associated. Top: These results correspond to the models that consider a limited number of species in the estimate, primarily anthropogenic sulphate. Note that the estimates do not vary widely, having converged to an approximate average value of –1.4 W $m^{-2}$, with a narrow standard deviation. Bottom: These results correspond to studies that include a variety of aerosol compositions and mixtures. Note that in contrast with cases shown in a), the estimates here indicate a larger range. This range can be the result of several factors, including different treatment of aerosol-cloud interactions but also other model biases.

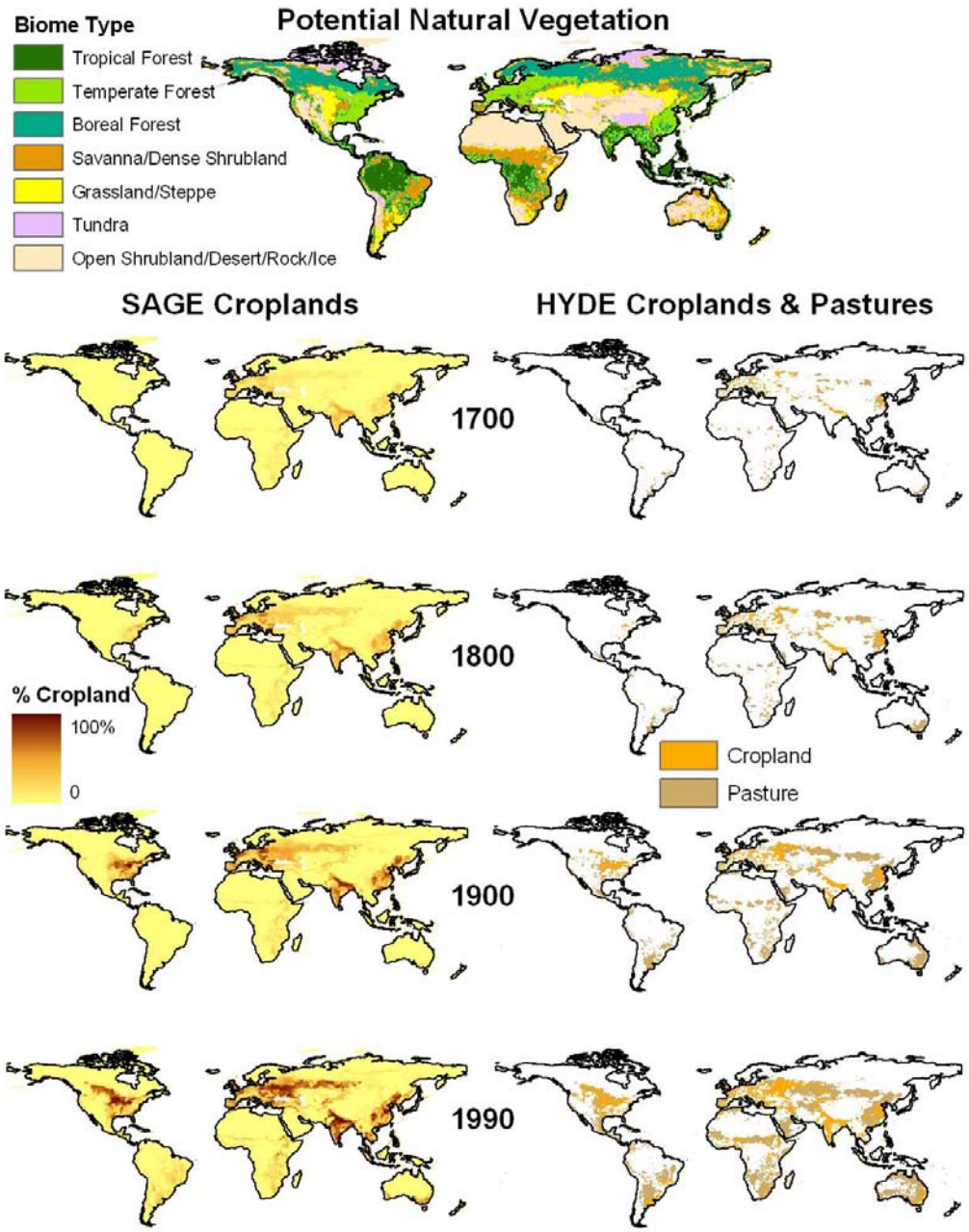


**Figure 2.17.** Anthropogenic modifications of land cover up to 1990. Top panel: Reconstructions of potential natural vegetation (Haxeltine and Prentice, 1996). Lower panels: reconstructions of croplands and pasture at 1700, 1800, 1900 and 1990. Left-hand column: fractional cover of croplands from SAGE (Centre for Sustainability and the Global Environment, University of Wisconsin; Ramankutty and Foley, 1999), at 0.5° resolution. Right-hand column: reconstructions from the HistorY Database of the Environment (HYDE), RIVM, Netherlands (Klein Goldewijk, 2001), with one land cover classification per 0.5° grid box.

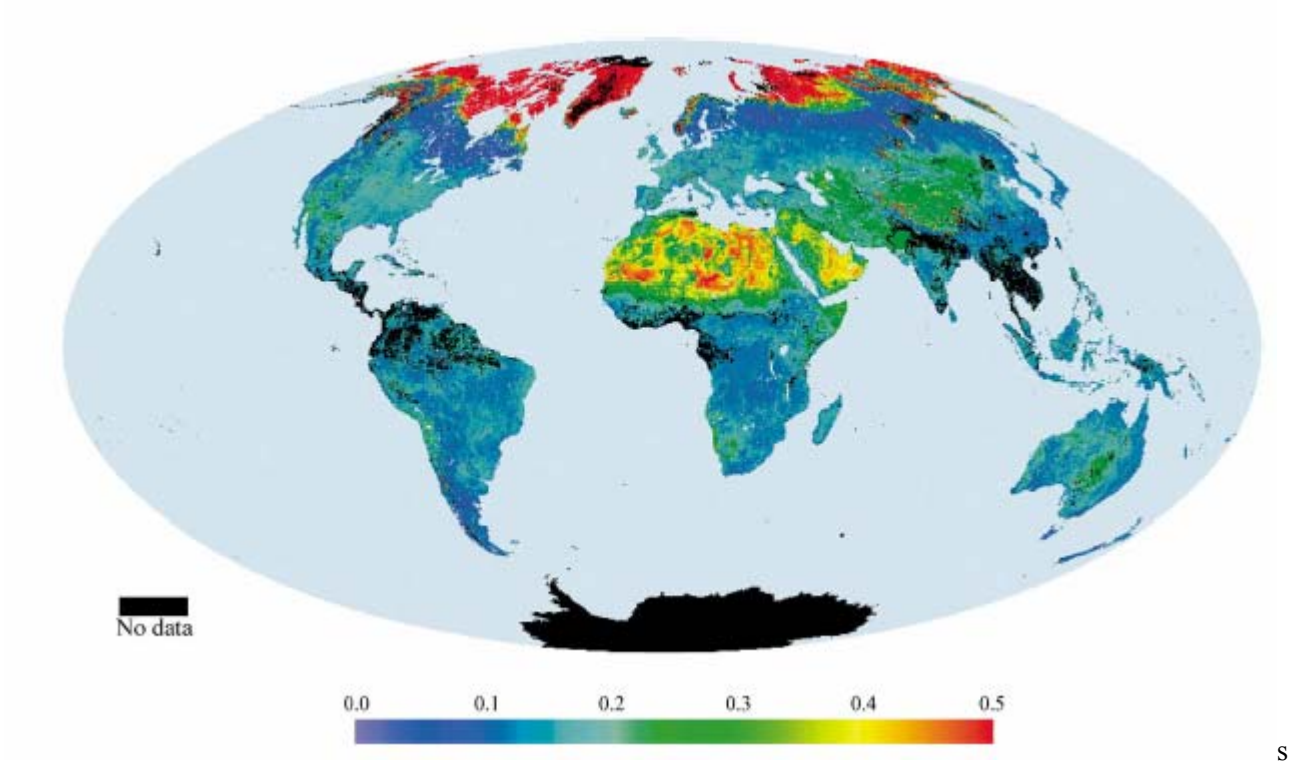


s

**Figure 2.18.** Surface albedo from the MODIS instrument (Schaaf et al., 2002). Global broadband white-sky albedo (0.3–5.0μm) for the period 9–21 May 2001. 20 km resolution for display purposes. Black indicates areas with no data, e.g., due to cloud cover

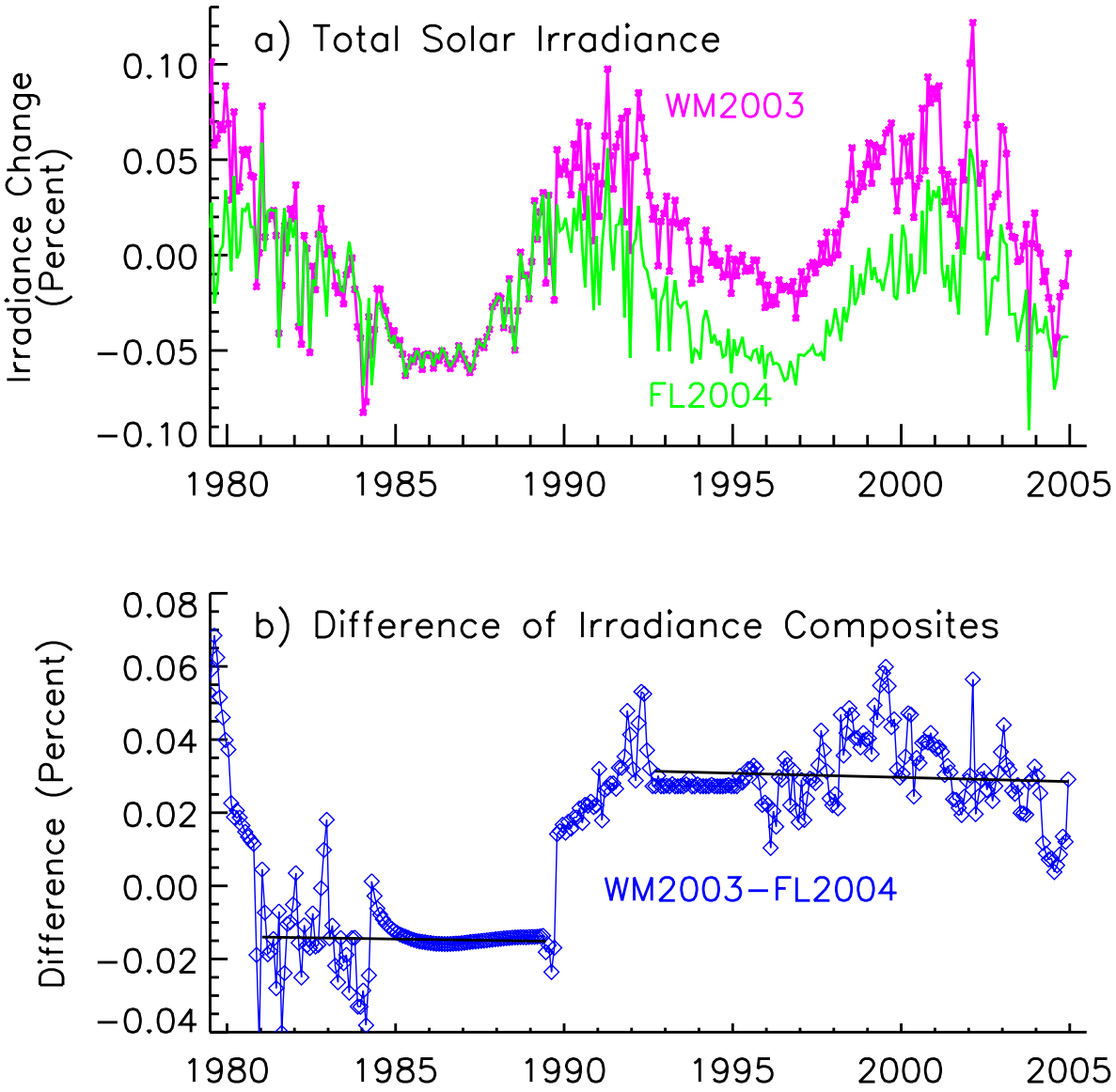


**Figure 2.19.** Compared in a) are percentage changes in monthly values of the irradiance composites of Willson and Mordvinov (2003) (WM2003, red symbols) and Fröhlich and Lean (2004) (FL2004, green solid line). The differences of the two composite records, also in percentages, shown in b), have no significant trend between January 1981 and June 1989, nor after August 1992. For these two time periods, the slopes of the solid lines (percent per month) are, respectively –0.0001 ± 0.0003 and –0.0002 ± 0.0002. The ~3-year jump from mid 1989 to mid 1992 produces higher irradiance levels in 1996 relative to 1986. Rather than a "secular "trend" over the past two decades, the upward trend in the WM2003 composite is likely of instrumental origin.

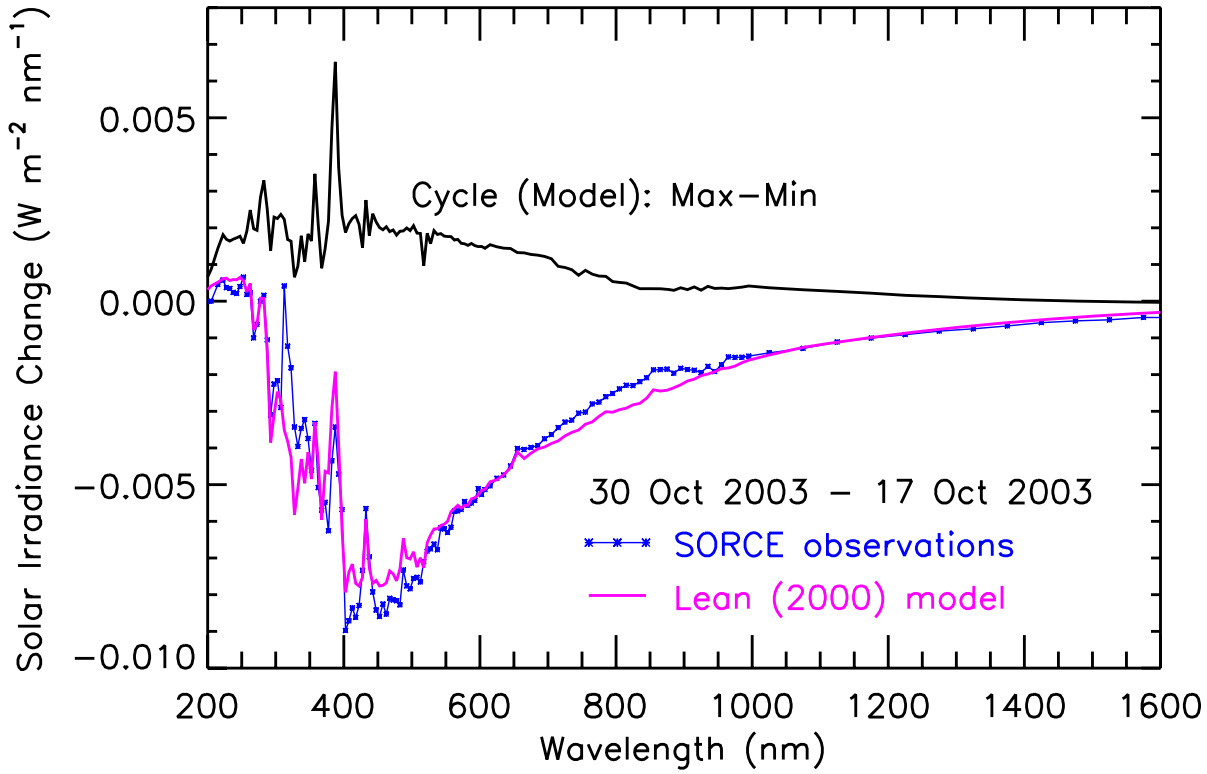


**Figure 2.20.** Shown are solar spectral irradiance energy changes from the maximum to minimum of the activity cycle (respectively, November 1989 and September 1986), estimated by a model of sunspot and facular effects (Lean, 2000). Also shown are the irradiance energy changes caused by significant solar activity on 30 October, relative to quieter conditions on 17 October, estimated by the model, compared with observations made by SIM on SORCE.

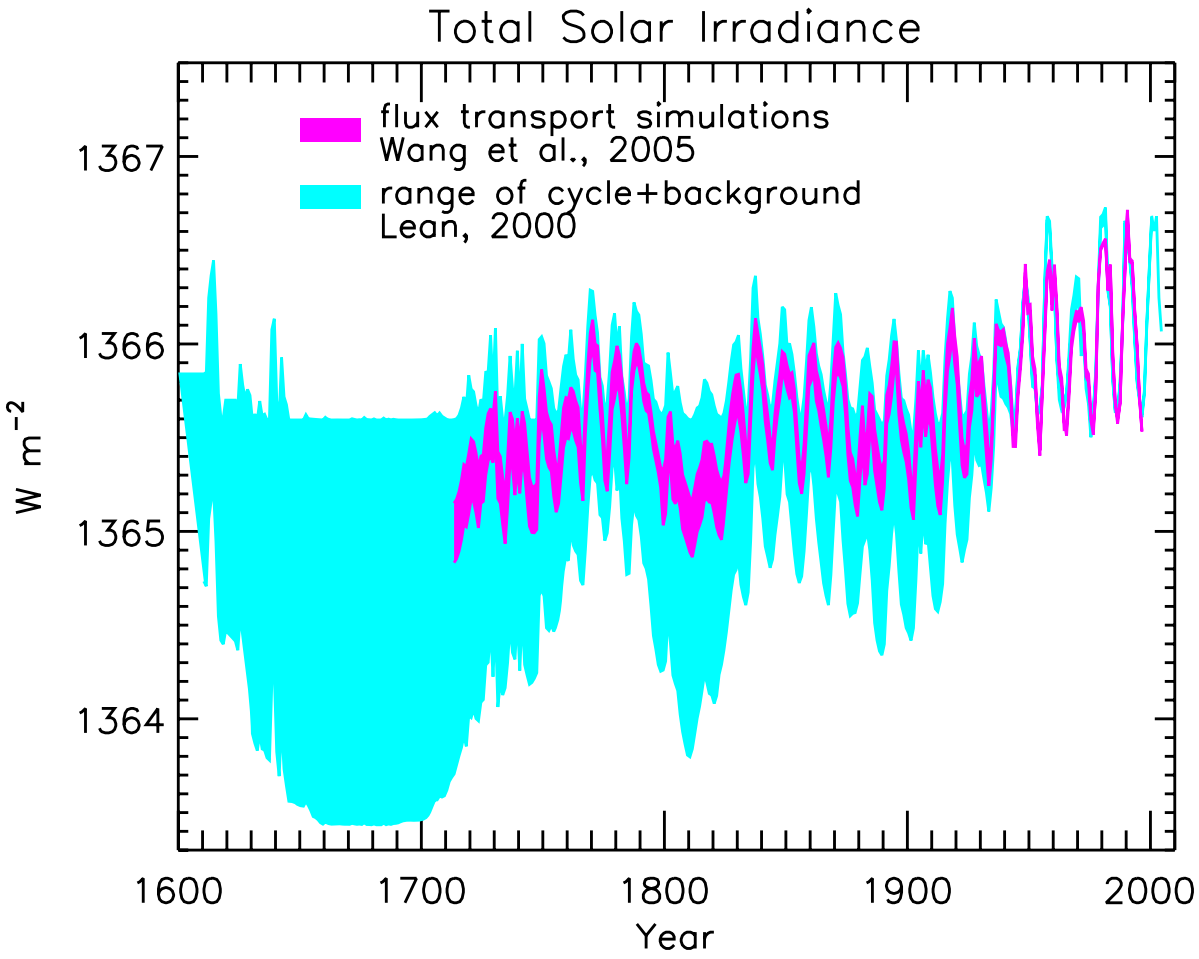


**Figure 2.21.** Shown as the upper envelope of the shaded region are total solar irradiance variations arising from the 11-year activity cycle. The lower envelope is the total irradiance reconstructed by Lean (2000), in which the long-term trend was inferred from brightness changes in Sun-like stars. In comparison the recent reconstruction of Wang, Lean, and Sheeley (2005) is based on solar considerations alone, using a flux transport model to simulate the long-term evolution of the closed flux that generates bright faculae.

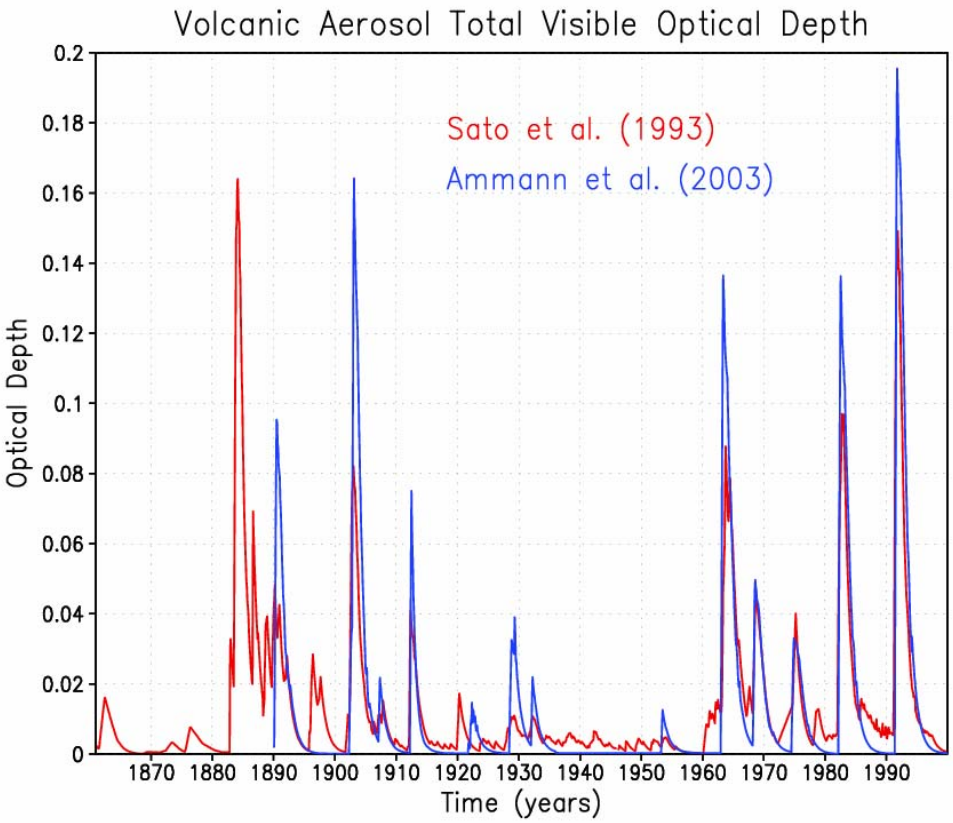


**Figure 2.22.** Visible (wavelength of 0.55 micron) optical depth estimates of stratospheric sulfate aerosols formed in the aftermath of explosive volcanic eruptions that occurred between 1860 and 2000. Results from two different datasets used in recent climate model integrations are shown. Note that Ammann et al. (2003) data begins in 1890.